scientific reports

OPEN

Aortic thrombi microstructure through contrast-enhanced X-ray microtomography

Joris Léonet[1], Jérôme Vicente[2], Mariangela De Masi-Jacquier[1,3] & Valérie Deplano[1]✉

The intraluminal thrombus (ILT) is a heterogeneous porous medium made up of three layers (luminal, medial, abluminal), found in most abdominal aortic aneurysms (AAA). Few morphological studies exist, and its role in disease progression remains controversial. Histological investigations suggest a harmful effect, leading to aortic wall hypoxia and potential rupture. However, 2D morphological studies cannot provide precise answers due to the complexity of ILT porosity. This study aims to provide reliable quantitative 3D morphological data using contrast-enhanced X-ray micro-computed tomography (micro-CT). We propose a validation pipeline for micro-CT image segmentation using virtual tomography. Our results show a decrease in porosity from the luminal to the abluminal layer, with similar pore diameters but more interconnected pores in the luminal region. The size of interconnected pores around 15–20 μm suggests cell passage is facilitated through the ILT's porous network. Finally, pore anisotropy was observed across the ILT thickness. This work suggests further studies on ILT permeability to validate its involvement in wall hypoxia.

Keywords Biological porous media, Micro-CT, Virtual tomography, Microstructure

The aorta is the main artery responsible for distributing blood throughout the body. An abdominal aortic aneurysm (AAA) is a localized dilation of the aorta in its abdominal section. This vascular pathology arises from an adverse remodeling of the aortic wall, which causes the artery to expand progressively. An intraluminal thrombus (ILT) commonly forms within the aneurysm[1,2]. This thrombus is an inhomogeneous, porous, multilayered medium which consists of cellular elements, such as red blood cells (RBC), white blood cells (WBC) and platelets (PLT), trapped in a fibrin network. Although the presence of ILT is suspected to contribute to AAA rupture by altering cellular activity, leading to aortic wall hypoxia[3] and structural weakening[1], its exact impact remains unclear. This uncertainty stems from limited experimental data and an urgent need to better understand ILT's microstructure and assess the potential transfer or transport of globular elements and cells through the ILT from the arterial lumen to the arterial wall.

Imaging soft biological tissues such as ILT is a common practice in the medical field, using techniques such as magnetic resonance imaging (MRI)[4–6], computed tomography (CT)[7,8], and histology[2,9,10]. These techniques provide valuable information on the general morphology, (micro)structure, and composition of tissues. However, they each have limitations including low spatial resolution, which ranges from 0.6 mm in CT to 2 mm in MRI, low tissue absorption in CT, the restriction to 2D microstructure information in histology, and labor-intensive experimental protocols. In recent years, new imaging techniques like laboratory X-ray micro-computed tomography (micro-CT) have been employed to achieve high-resolution 3D morphology in order to obtain more accurate qualitative and quantitative data. Using traditional X-ray absorption methods can be challenging due to the low contrast of biological tissues, affecting the image quality. For this reason, most studies enhance image quality by preparing their samples through fixation (in formaldehyde), dehydration (in ethanol baths), and staining (typically with phosphotungstic acid) or drying processes[10–13]. However, these methods alter the morphological and mechanical properties of the tissues[14,15]. Although advanced equipment like synchrotron could provide better imaging of soft tissues using phase-contrast imaging technique, access to such facilities is limited. Based on these findings, we developed a new preparation protocol in order to accurately visualize the ILT under laboratory micro-CT at high-resolution while maintaining the physiological tissue properties[16].

In order to perform reliable quantitative studies on this complex heterogeneous porous structure, a post-processing (filtering, segmentation, etc.) step is required for the micro-CT images. Images present a wide range of artifacts, including noise and systematic issues like blur, which complicate post-processing, especially during

[1]CNRS, Centrale Méditerranée, IRPHE UMR 7342, Aix-Marseille Univ, Marseille, France. [2]CNRS, IUSTI UMR 7343, Aix-Marseille Univ, Marseille, France. [3]Department of Vascular Surgery, AP-HM, Timone Hospital, Timone Aortic Center, Marseille, France. ✉email: valerie.deplano@univ-amu.fr

the segmentation stage. Additionally, there is no existing data in the literature on the 3D morphological features of the ILT. These make the validation of the post-processing of micro-CT images particularly difficult. Only few studies provide justification and validation for micro-CT image processing methods. To our knowledge, the only studies that validate the post-processing of their micro-CT images use reference images, either synthetic or with very high resolutions, which are then altered by adding artifacts such as noise or circular artifacts[17–19]. A study compared the performance of different segmentation methods on three types of multiphase tomographic images that were obtained synthetically, using synchrotron (9.24 μm pixel size) and micro-CT (32 μm pixel size) in the context of water resources research[17]. Using a synthetic image provided several advantages, particularly the ability to alter an image with known properties. The alteration of this image included the addition of noise, blur, and circular artifacts. The results showed that for all three types of images, blur was the main cause of poor segmentation results, as other artifacts could be managed using Non-Local Means (NLM) filter for image denoising. Another work developed a method to validate the processing of micro-CT images for geological applications, specifically porous rocks[18]. Their approach was similar to the previous study[17], involving the alteration of 'real' images that are either virtually generated or experimentally obtained at high resolution (1.94 μm/voxel in their study) with tomographic artifacts. Moreover, they introduced a process to add artifacts to the 'real' image to simulate the tomographic imaging and reconstruction process. Their results demonstrated that this process produced images with textures and contrasts that are close to a real experiment. Building on this, a study used a similar approach, altering rock images to train a Deep Learning tool for segmentation[19]. Since the quantitative data of the ILT strongly depend on the post-processing pipeline, it is therefore obvious that there is a need to validate this post-processing.

Consequently, as the long term goal of our research is to provide a better understanding of the role of ILT in the progression of pathology by studying the impact of its porous structure on globular elements and cells, the present study first (i) developed a pipeline for validating our image segmentation through virtual images; and (ii) quantitatively characterized multiple human ILT samples, providing 3D geometric parameters of the porous phase using laboratory contrast-enhanced micro-CT.

Methods

ILT collection

In total, 4 ILT were collected from patients with AAA who underwent aortic open surgery repair, in the Aorta Center of La Timone Hospital (AP-HM, Marseille, France). This study was approved by the research ethics committee (Ref No. XJFXL8). Informed consent was obtained from all subjects and/or their legal guardian(s). All experiments were performed in accordance with relevant guidelines and regulations. Information regarding the patients are available in Table 1.

Sample preparation and micro-CT scanning

After removal, ILT were preserved in Dulbecco's Modified Eagle's Medium (DMEM) solution made of deionized water with DMEM powder (Sigma-Aldrich, USA) and supplemented with glucose (Sigma-Aldrich, USA), sodium bicarbonate (Sigma-Aldrich, USA) and L-glutamine (Sigma-Aldrich, USA) at 4 °C. Whenever possible, ILT samples were prepared and tested a few days after extraction; otherwise, they were frozen at − 20 °C for later testing. In total, two ILT were prepared and tested a few days after removal, while the other two were thawed at 4 °C for 12 h before preparation and testing. ILT images were obtained using X-rays micro-CT as described in a previous study[16]. Briefly after removal, cylindrical samples of roughly 3 mm diameter and 5 mm in height were cut into the ILT thickness using a scalpel keeping the 3 layers. Depending on the ILT size and quality, several samples were cut in each ILT resulting in 17 samples in total (see Table 1). Samples were then stained during 4 days in a solution of DMEM and sodium polytungstate (SPT) (Sigma-Aldrich, USA) with a concentration of 15 g/L at 4 °C. Then, stained samples were placed in a polyimide tube filled with DMEM solution inside the microtomograph (Easytom XL, RX Solutions, Chavanod, France) for image acquisition. A 160 kV nano-focus source with a Tungsten (W) filament was used. The voltage and the current were set to 55 kV and 131 μ A, respectively. The ILT samples were placed at a 15.03 mm distance from the source and at a 620.5 mm distance from the imager. The 250×200 mm used imager had a detection area of 238×190 mm (pixel size of 12.7 μm), with a CsI scintillator layer. With this configuration, the final voxel size was 3 μm for all samples. A number of 5 averaged frames per projection was defined. Finally, 1120 projections were acquired in total for a scan duration of 3h22. After acquisition, volume datasets were obtained using XAct software (RX Solutions, Chavanod, France) for each ILT resulting in 17 datasets in total.

Label	Gender	Age	CT-scan		ILT			CVRF			
			AAA ϕ (mm)	ILT thi. (mm)	Frozen	TT (day)	No. of samples	HBP	SMO	CHOL	DIA
Patient 1	M	57	66	34	N	11	4	Y	Y	Y	Y
Patient 2	M	73	58	19	N	8	3	Y	Y	Y	N
Patient 3	M	62	55	29	Y	134	4	Y	Y	Y	Y
Patient 4	F	78	54	30	Y	112	6	Y	Y	Y	N

Table 1. Patient's data. Both AAA diameter and ILT thickness were obtained using CT-scan and taken as the maximum diameter and thickness, respectively. TT, maximum elapsed Time between harvesting and Test; CVRF, CardioVascular Risk Factors; HBP, High Blood Pressure; SMO, Smoking; CHOL, Cholesterol; DIA, Diabetes; Y, Yes; N, No

Micro-CT image post-processing

Each ILT volume dataset was analyzed using Dragonfly software (version 2022.2 for Linux) in order to identify their three layers. The differentiation between the layers was carried out at a macroscopic scale after ILT extraction, based on visual analysis of their colors, with the luminal layer appearing reddish, the medial layer whitish, and the abluminal layer yellowish[20,21]. After identification, maximum volume of interest (VOI) was defined for each ILT layer taking care of avoiding tissue artifacts such as tearing that can appears during cutting, that would modify the physiological ILT properties. Some abluminal regions were not imaged due to high delamination level resulting in 17 luminal, 17 medial, and 10 abluminal layers. Then, each VOI was extracted and exported in Fiji software[22] for Linux and segmented by thresholding. The selection of the threshold is described in section "Modelization of tomographic response". Finally, each binarized VOI was analyzed using iMorph software[23] for Linux to obtain the morphological properties of the ILT porous phase.

Modelization of tomographic response

We propose a digital workflow (Fig. 1) inspired by a previous study[18] to evaluate our segmentation technique based on virtual tomography. A 3D synthetic porous image ($400 \times 400 \times 400$ voxels) was generated using PoreSpy[24] toolkit within a Python environment (① in Fig. 1). As the objective was to mimic the ILT microstructure, we need to set a value of porosity creating a 3D synthetic image. A previous study found a mean porosity of 20% for all three ILT layers based on 2D histological images[1]. Porosity values comprised between 4% and 8% were obtained in our previous study[10] for abluminal and medial layers respectively, using phosphotungstic acid (PTA) staining protocol for ILT sample preparation. Based on these finding, a porosity of 10% was approximated for the 3D synthetic image in order to be as restrictive as possible, since small pores are the most complicated to visualize and segment. After binarization, this 3D image was called ground truth (GT). Using Astra-toolbox[25] within a Python environment, both forward projection and filtered back projection algorithms were computed on the GT, leading to raw images (② in Fig. 1). The projection geometry parameters, such as the distance between the source and the sample, the rotation or the cone-beam geometry, were defined to mimic our real tomographic acquisition conditions. Blur was added in order to mimic an artifact that can be encountered using cone-beam geometry, with an image appearing less sharp as you move away from the center[18]. Blur was varied with a kernel size between [1;3] voxels. Gaussian and Poisson noise were also added to the projections. The Gaussian noise simulates the noise generated by the detector and encountered during reconstruction, whereas the Poisson noise replicates the noise arising from the variations in the number of photons detected by the flat panel. To select the appropriate noise level, the parameters μ and σ of the Gaussian noise expression $p(x)$ were varied

$$p(x) = \frac{1}{\sqrt{2\pi\sigma^2}} e^{-\frac{(x-\mu)^2}{2\sigma^2}} \tag{1}$$

where μ is the average value of x and σ the standard deviation. Both parameters were varied between [0;4] and between [0;150] for μ and σ, respectively. The same procedure was conducted for the Poisson noise expression $f(k; \lambda)$

$$f(k; \lambda) = \frac{\lambda^k e^{-\lambda}}{k!} \tag{2}$$

with $f(k; \lambda)$ the Poisson distribution that describes the probability of k event in the interval λ. The parameter λ was varied between [0;120]. The range of values for artifacts were empirically selected. All artifacts were added during the projection step leading to noisy images. In order to compare grayscale histograms matching of micro-
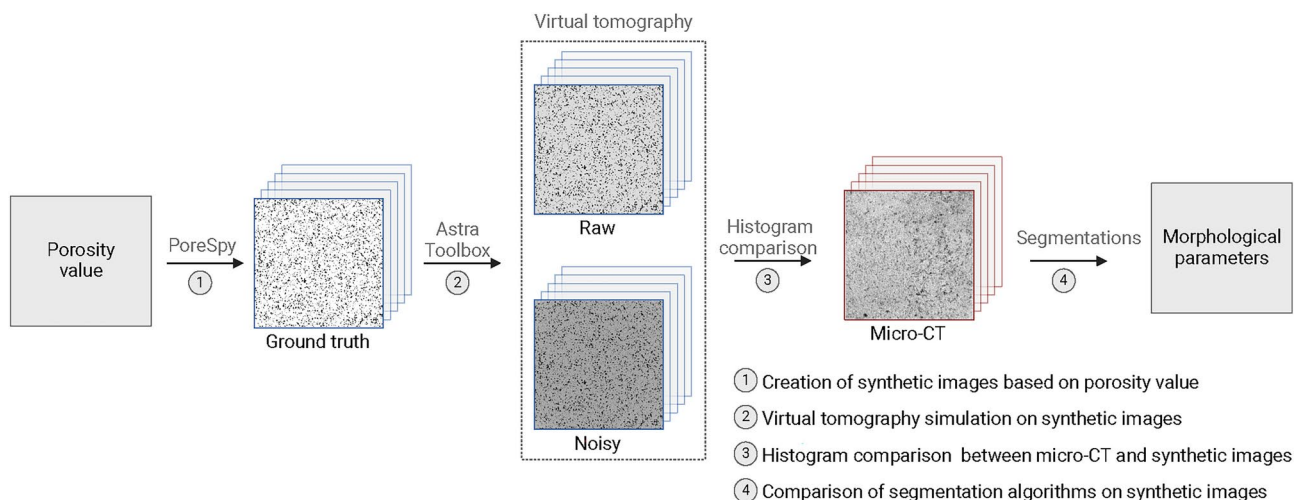

Fig. 1. Virtual tomographic response workflow.

Stack	Algorithm	Voxel count (voxel)	Porosity (%)	CC (voxel)	IoU (%)
GT	–	6448889	10.08	152068	100
	Otsu	8405573	13.13	173928	75.53
Virtual	Phansalkar	**7298135**	**11.4**	**143343**	**84.45**
	Weka	5503057	8.6	94248	69.98
	Otsu	**6718355**	**10.5**	128530	79.49
Virtual-NLM	Phansalkar	6125983	9.57	**133633**	**80.09**
	Weka	9260091	14.47	75295	60.06

Table 2. Morphological characteristics of the porous phase in synthetic images with (Virtual-NLM) and without (Virtual) applying a filtering process. CC and IoU stand for connected components count and intersection over union, respectively. The closest values to the GT are in bold.

		D_p	D_{10}	± Dif. (%)	D_{50}	± Dif. (%)	D_{90}	± Dif. (%)
GT	–	5.19 (1.21)	3.60	–	5.00	–	6.80	–
	Otsu	5.43 (1.24)	3.75	+ 4.2	5.30	+ 6	7.00	+ 2.9
Virtual	Phansalkar	5.31 (1.22)	**3.70**	+ 2.8	5.15	+ 3	**6.85**	+ 0.7
	Weka	**5.23 (1.11)**	**3.70**	+ 2.8	**5.10**	+ 2	6.65	− 2.2
	Otsu	5.24 (1.17)	3.70	+ 2.8	5.10	+ 2	**6.70**	− 1.5
Virtual-NLM	Phansalkar	**5.20 (1.16)**	**3.65**	+ 1.4	**5.05**	+ 1	**6.70**	− 1.5
	Weka	5.61 (1.21)	3.95	+ 9.7	5.50	+ 10	7.10	+ 4.4

Table 3. Equivalent pore diameter size (voxel) distributions expressed in terms of percentage of pore volume. The difference of each characteristic diameter D_{10}, D_{50} and D_{90} is compared to the GT and expressed in percentage. The closest values to the GT are represented in bold.

CT and noisy virtual images, three metrics were calculated using OpenCV including Correlation, Intersection and Bhattacharyya distance similarities (③ in Fig. 1). The Intersection measures the common area between two histograms while the Bhattacharyya distance measures the distance between two probability distributions. Finally, different segmentation algorithms were applied to the noisy images using Fiji software and compared (④ in Fig. 1). A wide range of algorithms exist but after initial testing, only three were selected based on visual inspection including Otsu auto-local thresholding[26], Phansalkar auto-local thresholding[27] and Trainable Weka Segmentation 2D[28]. The other algorithms were considered unsuitable for segmenting our porous structure. The efficiency of a NLM filter[29] was also investigated before segmentation as it is one of the most commonly used denoising filter[30]. To compare all segmentation approaches, the geometrical properties and accuracy were calculated as presented in Table 2. Using iMorph software, we measured the total number of voxel (*voxel count*) for the porous phase, the *porosity*, and the *connected components count (CC)* which represents the number of connected regions calculated using a 26-neighborhood connection algorithm. Moreover, we calculated the pore size distribution (PSD) with mean pore diameter D_p and characteristic diameter D_n (Table 3). The PSD was expressed in function of cumulative volume (Q3)[31]. The metric D_n represents the pore diameter such that n% of the volume distribution consists of pores smaller than this diameter, while $(100-n)$% consists of pores larger than it[31]. Then, the parameters D_{10}, D_{50} and D_{90} were calculated in order to investigate the impact of segmentation on small, medium and large pores, respectively[31]. Finally, the segmentation accuracy was measured using the *intersection over union (IoU)* metric, which is a measure of the overlap between two segmentations, comparing the different segmentations to the GT in our case.

Statistical analysis
Analysis of normality of the obtained morphological properties was performed using Shapiro-Wilk test and assumed for $P > 0.05$. Then, equality of variances was evaluated using Levene's test and assumed for $P > 0.05$. Morphological data for each ILT layer obtained via micro-CT were compared to assess potential differences between the layers. This analysis involved a Kruskal-Wallis test, followed by a post-hoc Dunn's test. All statistical analyses were conducted using BioRender that uses R (version 4.2.2).

Results
Grayscale histograms matching
Several noise levels were empirically tested to obtain a matching between experimental and virtual grayscale histograms. The results presented in Fig. 2 show the best matching when a Gaussian noise with $\mu = 0$ and $\sigma = 4$, a Poisson noise with $k = 120$ and $\lambda = (600, 1120, 600)$, and a blur with a kernel size of 1 were added. Even if noisy virtual and micro-CT grayscale histograms are highly similar, there is a noticeable difference in the frequency of low gray levels. The noisy virtual histogram shows a slightly higher frequency of low-intensity pixels compared to the micro-CT images. This indicates that the noisy images contain more low-intensity pixels.
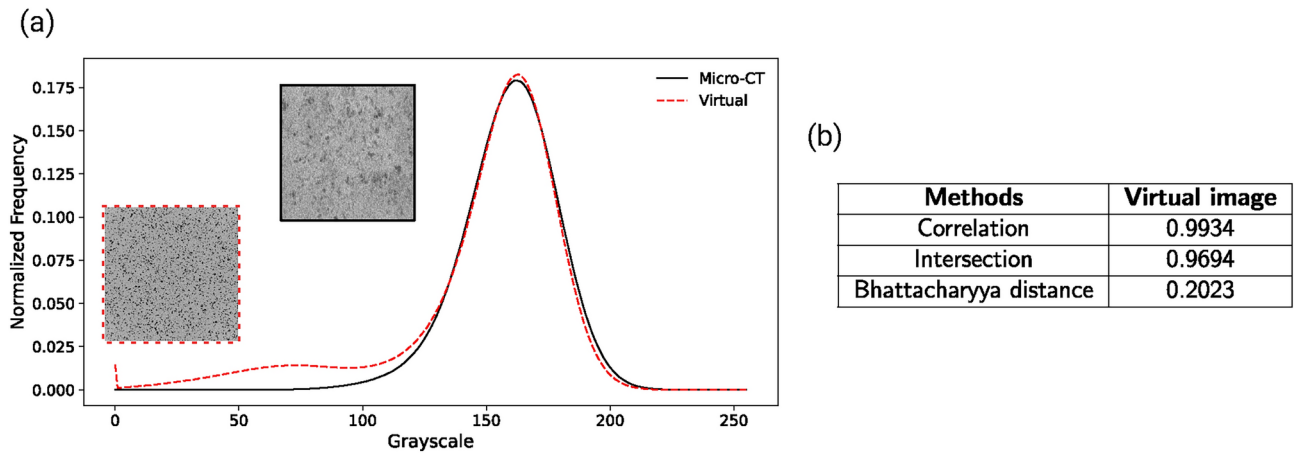
(a)

(b)

Methods	Virtual image
Correlation	0.9934
Intersection	0.9694
Bhattacharyya distance	0.2023

Fig. 2. (**a**) Comparison data between micro-CT and noisy virtual grayscale histograms. The micro-CT histogram comes from the volume dataset obtained experimentally. The virtual images had a kernel size of 1 for blur, a Gaussian noise with $\mu = 0$ and $\sigma = 4$, a Poisson noise with $k = 120$ and $\lambda = (600, 1120, 600)$. (**b**) Evaluation metrics comparing micro-CT and noisy virtual images. All metrics are comprised between 0 and 1 with 1 the best match for Correlation and Intersection while 0 is the best match for Bhattacharyya distance.

Efficiency of segmentation approaches through morphological properties

The morphological properties of the virtual tomographic stack were calculated and compared to the GT. The impact of a NLM filter on the morphological properties was also investigated. The results presented in Table 2 show that Phansalkar algorithm effectively segments the porous phase of reconstructed stacks with approximately 84.5% accuracy. Moreover, we observed that Otsu algorithm tends to over-segment the pore with a fraction of 13.13% compared to 10.08% for the GT. In opposite, the Weka algorithm tended to sub-segment the pore with a fraction of 8.6%. When a NLM filter was applied prior to segmentation, we observed that both the Phansalkar and Otsu algorithms performed similarly, with an accuracy of approximately 80% (Table 2), which was lower compared to the results obtained without filtering. To evaluate the impact of segmentation on the porous phase, the PSD and D_{10}, D_{50}, and D_{90} parameters were calculated (Table 3) and plotted to better visualize the results for all segmentation techniques (Fig. 3). Globally, we observed a higher mean equivalent pore size for all segmentations compared to the GT, where Phansalkar algorithm seems to be the most accurate in most cases with a maximum deviation of 3%. Then, we can see an over-segmentation for all three algorithms in the case of small (D_{10}) and medium (D_{50}) pore sizes with a maximum difference of +10%. This over-segmentation can be observed in Fig. 3a with a shift of the curves toward higher equivalent diameters. In the case of large (D_{90}) pore sizes, alternating over- and under-segmentation was observed, where under-segmentation was preferentially observed with a NLM filter. Taking into account the drop in overall segmentation quality with the use of an NLM filter observed previously, we see that both Phansalkar and Weka algorithms have the most accurate results. Finally, when looking at the overall results, we concluded that Phansalkar algorithm without NLM filter is the most appropriate algorithm for the segmentation of our micro-CT images.

Morphological analysis of ILT micro-CT images

Representative results are presented in Fig. 4, showing a macroscopic view of both ILT and sample after cutting (Fig. 4a), a micro-CT image of ILT thickness at 3 μm resolution (Fig. 4b), and porosity maps for all layers (Fig. 4c). Qualitatively, we observed several gray levels and porous structures over the entire thrombus thickness (Fig. 4b), corresponding to the different ILT layers. The various gray levels are due to the different ILT constituents such as RBC, WBC, PLT and fibrin. Looking to the porous structures (Fig. 4c), we observed different geometries between layers, highlighted by the pore interconnection calculated using the 26-connectivity algorithm and represented by the color in Fig. 4c. The luminal layer seems to be highly interconnected over the entire thickness (pink color in Fig. 4c). Concerning the medial layer, a different porous structure was observed with less interconnection compared to the luminal layer. Finally, the abluminal layer presents a lower pore interconnection compared to both luminal and medial layers.

Quantitative analysis on the porous phase was conducted with the aim of comparing all three ILT layers (Fig. 5a). First, mean porosity with standard deviation (SD) was calculated for each layer. The results demonstrated mean values of 11% (SD 3.7), 9.6% (SD 3.8), and 8% (SD 2.6) for luminal, medial and abluminal layers, respectively. The PSD results demonstrated D_p values between 15 and 20 μm with no significant difference between all layers (Fig. 5b). Then, mean values of 15 μm, 25 μm and 40 μm were obtained for D_{10}, D_{50} and D_{90}, respectively with no significant difference between layers (Fig. 5b). The level of anisotropy was calculated using the Mean Intercept Length (MIL) approach in x, y and z directions. This technique involves measuring the average distance between intersections of test lines with the solid-pore interface, providing a directional analysis of the microstructure. Micro-CT images of the samples were analyzed by superimposing parallel test lines along the principal orthogonal directions (x, y, and z axes). For each direction, the number of intersections between the test lines and the pore boundaries was counted, and the MIL was calculated making the ratio between the total
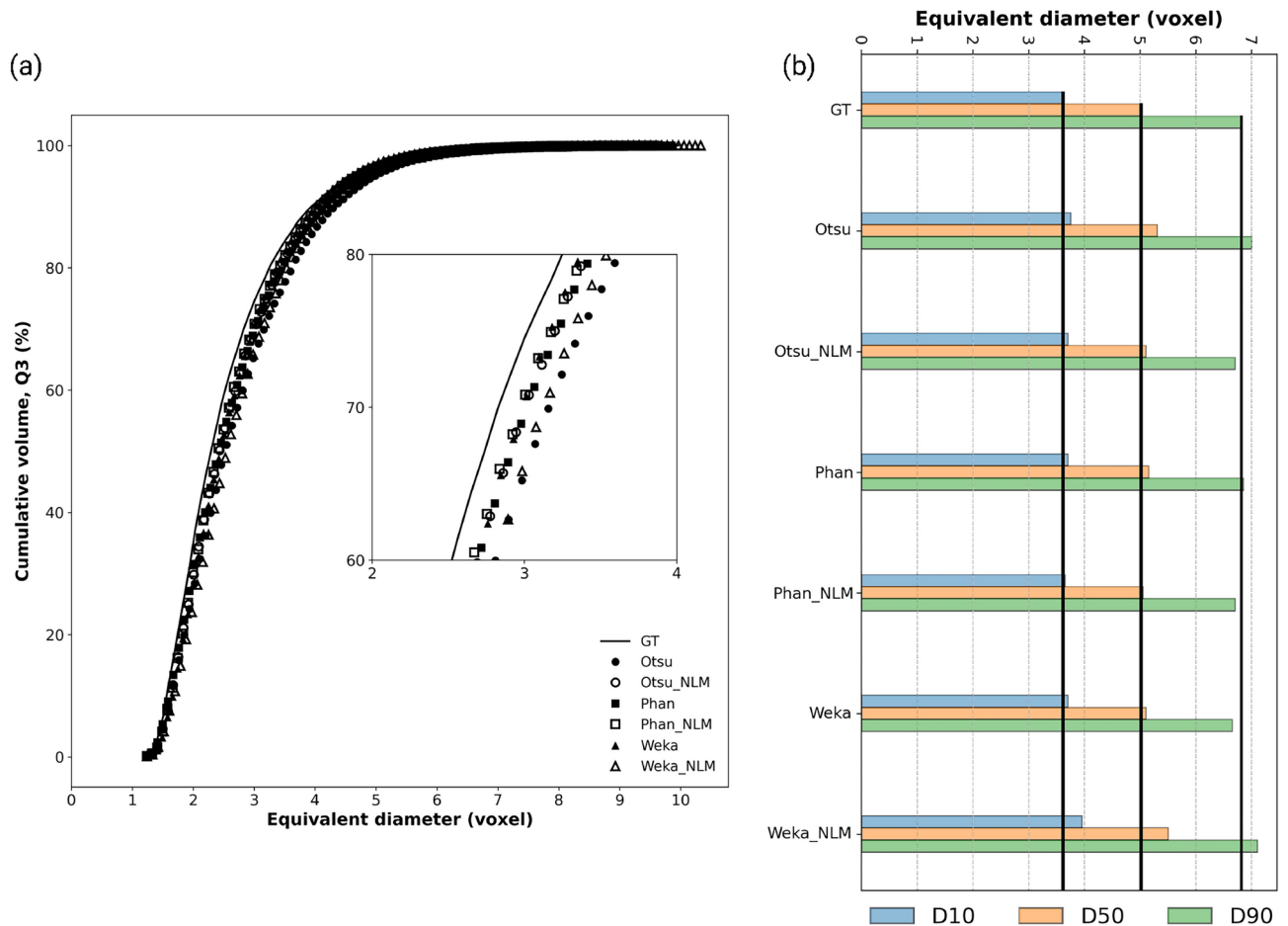
Fig. 3. (**a**) PSD expressed in percentage of cumulative volume (Q3) for noisy images. (**b**) Histograms of the pore size equivalent diameters D_{10}, D_{50}, and D_{90} of noisy images. The three vertical solid lines represent the GT values for D_{10}, D_{50} and D_{90}. Created with Python Language Reference, version 3.8., available at http://www.python.org.

length of test lines and the number of intersections. By calculating the MIL ratios x/y, x/z and y/z, the level of pore anisotropy was quantified where a value of 1 corresponds to isotropy. We observed that the porous structures in x and y directions are highly similar leading to an isotropic morphology (Fig. 5c). However, when considering the z-direction corresponding to ILT thickness, anisotropy was detected, with statistically significant differences observed: $P < 0.0001$ for both luminal and medial layers, and $P < 0.001$ for the abluminal layer (Fig. 5c). Finally, we showed that the maximum interconnected pore volumes are located in the luminal region even if no statistical difference was observed between layers (Fig. 5d). Moreover, a very high variability was observed for all types of layer due to the patient-specificity aspect.

Discussion

In this study, we highlighted the lack of a method for validating micro-CT images of thrombi, leading to the development of a validation workflow based on previous works[18,19], using a synthetic 3D image mimicking the ILT microstructure. With the use of virtual tomography, we were able to generate virtual images with grayscale levels similar to those obtained from human ILT images, and used to evaluate several segmentation algorithms where Phansalkar auto-local thresholding was found the most accurate. Based on this, the 3D morphological properties of the ILT porous phase were assessed computing several parameters such as porosity (ϕ), PSD (D_p; D_n), level of anisotropy, and pore connectivity (P_{co}).

Thanks to the developed workflow, we provide a new approach for validating contrast-enhanced micro-CT images of soft biological tissues in general, currently non-existent in the literature. In fact, the accurate segmentation of low-contrasted tissue is particularly complicated. Actually, the choice of segmentation method for images of this type is often made arbitrarily, based on visual qualitative criteria, raising questions about the validity of the results.

Through the morphological study, we obtained, for the first time, reliable 3D results on the ILT's porous structure, particularly thanks to the image validation method using micro-CT. Indeed, the few studies focusing on the microstructure of ILT are mostly based on 2D images obtained through histology[1–3,9,10] or SEM[32–34]. However, due to the complexity of the ILT's porous microstructure, it is impossible to accurately estimate
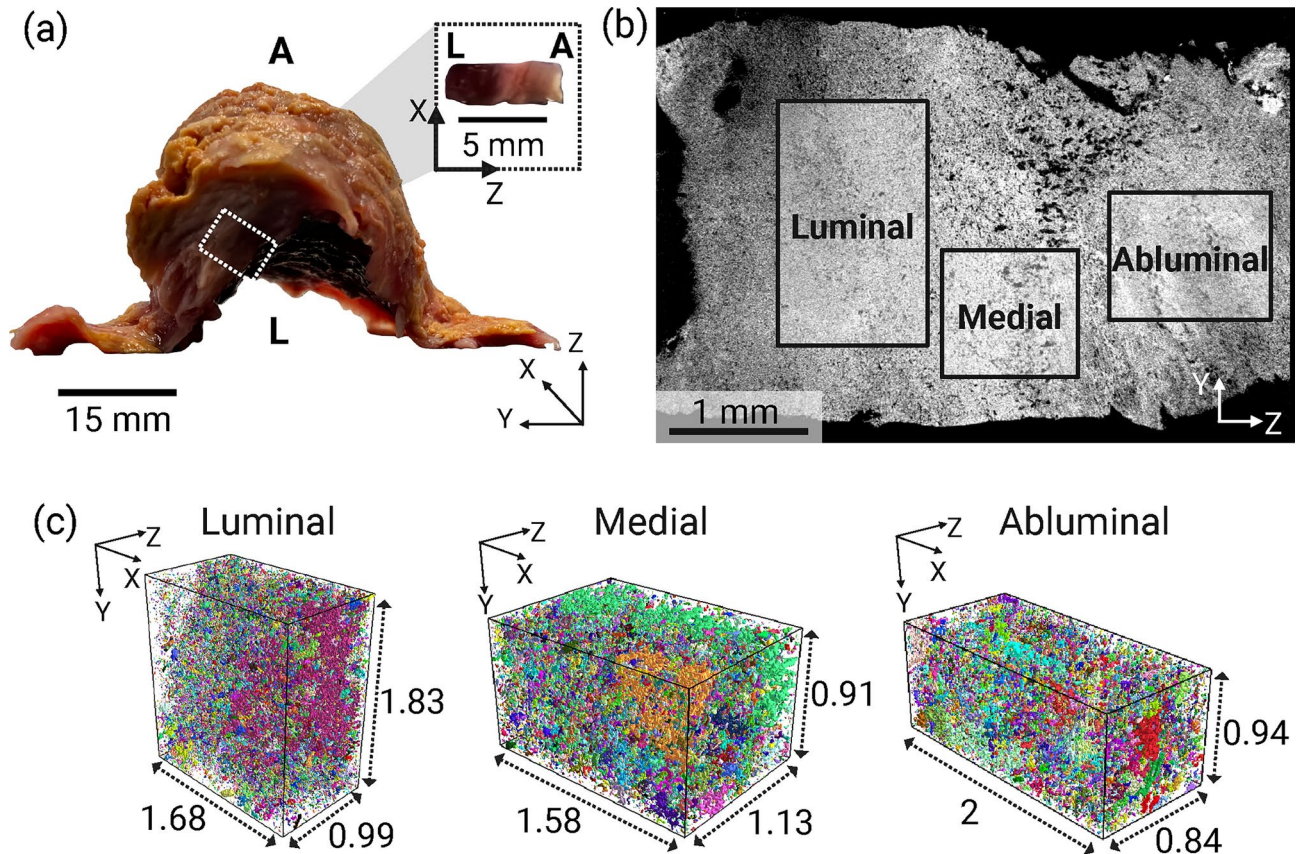
Fig. 4. Representative micro-CT results. (**a**) Macroscopic view of the ILT (Patient 3) after extraction with a sample cut through the ILT thickness, showing the different layers where *L* and *A* stand for *luminal* and *abluminal*, respectively. (**b**) 2D micro-CT slice of the sample showing the different structures for all layers. One VOI was defined for each ILT layer using Dragonfly software, version 2022.2 (https://www.theobjects.com/dragonfly). (**c**) 3D porosity maps for all ILT layers obtained using 26-connectivity algorithm from iMorph software, version 2022.09 (https://imorph.sourceforge.net/). Colormap: each color corresponds to a unique interconnected pore network.

quantitative parameters that are porosity (ϕ), mean pore diameter (D_p) or level of interconnection (P_{co}). Only very few studies provided quantitative morphological data regarding the ILT's porous phase[1,9]. In this work, we have found a mean pore diameter of around 15–20 μm in all layers (D_p). A previous histological work quantitatively observed pore areas for each layer and showed a high density around 500 μm^2 ($D_p \approx 12.6$ μm) for all three layers[1]. No significant difference was found between luminal and medial layers, compared with the abluminal that showed higher density around 600 μm^2 ($D_p \approx 13.8$ μm) and 3000 μm^2 ($D_p \approx 30.9$ μm). Compared to our results, their calculated mean D_p for both the luminal and medial layers are similar to our observations, except for the abluminal layer, where their value is significantly higher. Moreover, a previous morphometric study using histology identified pores with areas smaller than 5 μm^2 ($D_p \approx 1.3$ μm), potentially permitting macromolecular passage, as well as larger pores exceeding 36 μm^2 ($D_p \approx 3.4$ μm), which may facilitate cellular passage[9]. They also observed an increase in pore area from the luminal to the abluminal layers, with a porous network that may be interconnected. Similarly, we identified significant amount of pores with $D_p \approx 3.5$–4 μm although pores with $D_p < 3$ μm were not visible, as our spatial resolution was 3 μm. We also confirmed the presence of interconnected pore networks highlighted in a previous work[9], providing quantitative details on pore connectivity, showing that the largest average interconnected porous network represents approximately 50%, 35%, and 30% of the total volume of the luminal, medial, and abluminal layers, respectively. The differences observed in the mean D_p between our work and previous histological studies could be attributed to several factors, including the sample preparation for histology, which significantly alters the ILT microstructure, the image processing technique used to eliminate pores smaller than 14 μm[1], and the use of 2D images that fail to capture the actual complex porous microstructure. With the size of the observed interconnected porous networks in this study, we can hypothesize that these networks facilitate cell passage, with cellular diameters that can vary from 2 μm (PLT) to 15 μm (WBC). Furthermore, our results indicate a decrease in porosity, with no significant statistical difference, from the luminal to the abluminal layer, consistent with findings from a previous study[1]. However, their reported values (23.3%, 22.9%, and 19.6% for the luminal, medial, and abluminal layers, respectively) were higher than those observed in our study (11%, 9.6%, and 8% for the same regions). These differences can be explained by the high heterogeneity between patients (Fig. 5a), by the image
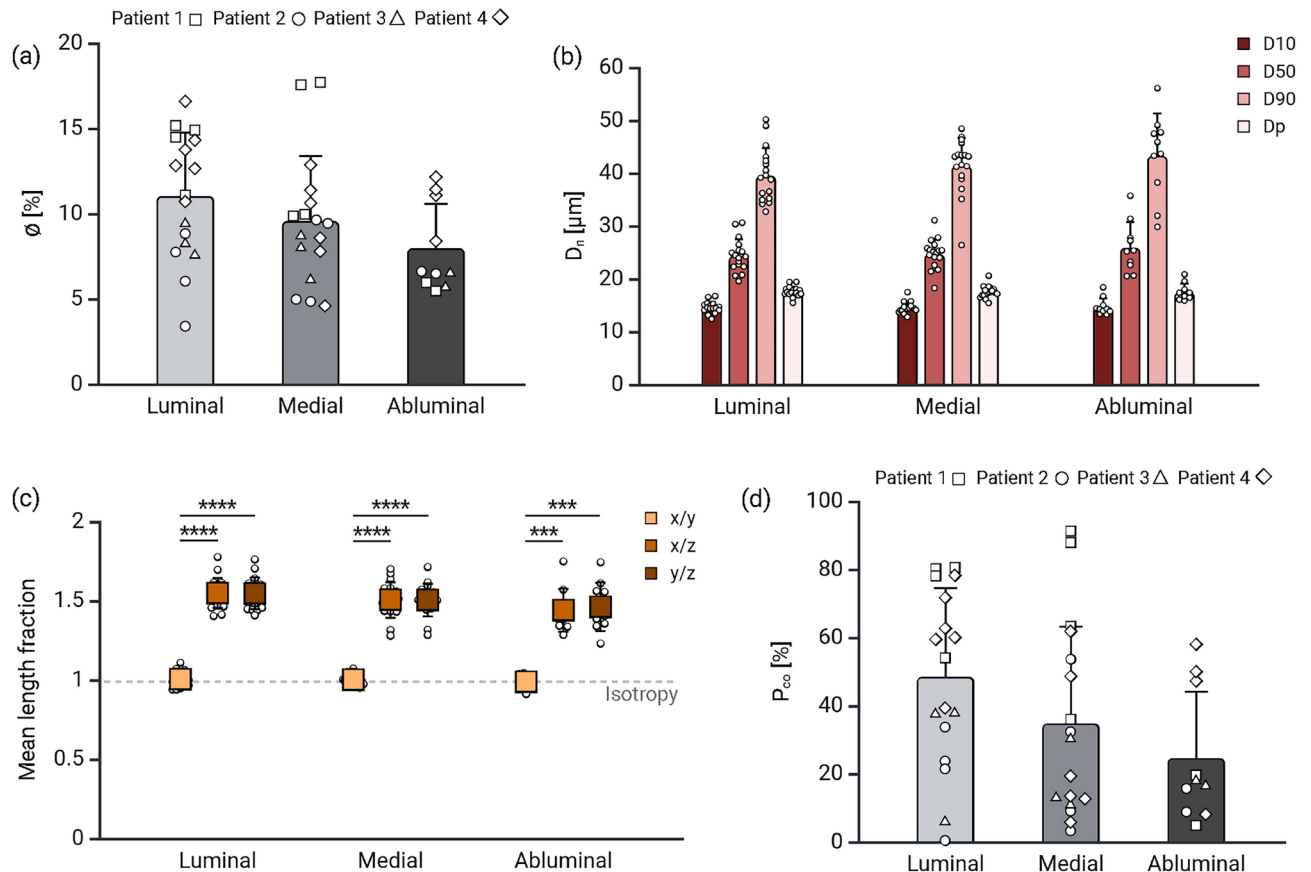
Fig. 5. Quantitative data on the ILT porous phase. (**a**) Porosity values for each ILT layer. (**b**) Pore size distribution of mean D_n with standard deviation for each ILT layer. (**c**) Mean length fraction between all axis for each ILT layer. (**d**) Mean P_{co} with standard deviation for each ILT layer. $n = 17$ for both luminal and medial layers while $n = 10$ for the abluminal layer. $^*p < 0.05,^{**}\,p < 0.01,^{***}\,p < 0.001,^{****}\,p < 0.0001$. Luminal, medial and abluminal layers were compared using Kruskal-wallis test followed by Dunn's test. Created with BioRender.com.

processing and finally the use of 2D altered histological images. Nevertheless, we did not conduct a patient-wise analysis as our cohort (4 patients) is too small. The only existing 3D data obtained using micro-CT images were previously published by our group for one patient showing porosities of 7.4%, 8.2%, and 4% for luminal, medial and abluminal layers, respectively[10]. However, these results were obtained using a preparation protocol that damages the tissue structure with formalin solution and ethanol[16], thus calling into question the reliability of the results. Finally, to our knowledge, this study is the only one to quantify the anisotropy of the different ILT layers, showing a porous anisotropy in the z-direction that corresponds to the ILT thickness. This anisotropy could originally come from the deposition of different layers over time. These morphological parameters are essential for a better understanding of the role of the ILT in pathology, particularly its potential contribution to wall hypoxia. Histological studies observed the presence of cells (RBC, WBC, PLT, etc.), primarily in the luminal layer, occasionally in the medial layer, and rarely in the abluminal layer[2,9,10]. However, it is essential to understand the mechanism(s) leading to the presence of these cells in the ILT, which may result from their entrapment due to the formation of successive layers or from the interconnection of pores, as highlighted in this study. A more comprehensive investigation into the permeability of the different ILT layers is necessary to validate this hypothesis, and finally to address the question of the ILT's role in vessel wall hypoxia.

Some limitations have to be mentioned. First, ILT samples from only four patients were tested, and additional samples are needed to potentially identify significant differences due to the high morphological heterogeneity within the same sample as well as between patients. However, obtaining human samples is currently challenging due to the low number of open surgeries performed in clinics since the advent of endovascular procedures. Our synthetic images were built in order to match a real human ILT structure as presented in Fig. 1. However, the ILT is made of three distinct layers each with its own structure[2,10,16], resulting in a porosity gradient that was not mimicked in the synthetic images.

Ongoing investigations aim to calculate the intrinsic permeability of each ILT layer based on micro-CT data and to establish correlations between pore interconnectivity and permeability. Additional experimental and numerical studies are required to elucidate cellular transport mechanisms such as diffusion and convection.

Ultimately, the objective is to develop a reliable ILT model, integrating morphological and mechanical properties, that can be incorporated into numerical simulations of AAA pathologies.

Conclusion

We developed a pipeline to validate the segmentation of micro-CT images of ILT using synthetic images and virtual tomography. Through this approach, we quantitatively characterized the ILT porous phase in 3D, revealing a decrease in both porosity (ϕ) and the maximum interconnected pore network (P_{co}) from the luminal to the abluminal layers. Notably, we provided the first quantitative evidence in the literature of pore anisotropy across the ILT thickness. This study offers morphological insights, particularly highlighting the presence of cells in the luminal layer with higher pore interconnection.

Data availability

The datasets used and/or analysed during the current study are available from the corresponding author on reasonable request.

References

1. Gasser, T. C., Martufi, G., Auer, M., Folkesson, M. & Swedenborg, J. Micromechanical characterization of intra-luminal thrombus tissue from abdominal aortic aneurysms. *Ann. Biomed. Eng.* **38**, 371–379 (2010).
2. Tong, J. & Holzapfel, G. A. Structure, mechanics, and histology of intraluminal thrombi in abdominal aortic aneurysms. *Ann. Biomed. Eng.* **43**, 1488–1501 (2015).
3. Vorp, D. A. et al. Association of intraluminal thrombus in abdominal aortic aneurysm with local hypoxia and wall weakening. *J. Vasc. Surg.* **34**, 291–299 (2001).
4. de la Motte, L. et al. Categorization of aortic aneurysm thrombus morphology by magnetic resonance imaging. *Eur. J. Radiol.* **82**, e544–e549 (2013).
5. Nchimi, A. et al. MR imaging of iron phagocytosis in intraluminal thrombi of abdominal aortic aneurysms in humans. *Radiology* **254**, 973–981 (2010).
6. Nguyen, V. et al. Abdominal aortic aneurysms with high thrombus signal intensity on magnetic resonance imaging are associated with high growth rate. *Eur. J. Vasc. Endovasc. Surg.* **48**, 676–684 (2014).
7. Labruto, F., Blomqvist, L. & Swedenborg, J. Imaging the intraluminal thrombus of abdominal aortic aneurysms: Techniques, findings, and clinical implications. *J. Vasc. Interv. Radiol.* **22**, 1069–1075 (2011).
8. Arbănaşi, E. M. Computed tomography angiography markers and intraluminal thrombus morphology as predictors of abdominal aortic aneurysm rupture. *Int. J. Environ. Res. Public Health* **19**, 15961 (2022).
9. Adolph, R. et al. Cellular content and permeability of intraluminal thrombus in abdominal aortic aneurysm. *J. Vasc. Surg.* **25**, 916–926 (1997).
10. Léonet, J. *et al.* Morphological and poro-mechanical characterization of thrombi from aortic aneurysm. In *47ème Congrès de la société de biomécanique* S5186–S5188 (2022).
11. Dumitriu LaGrange, D. et al. MicroCT can characterize clots retrieved with mechanical thrombectomy from acute ischemic stroke patients: A preliminary report. *Front. Neurol.* **13**, 824091 (2022).
12. Karagiannidis, E. et al. Micro-CT-based quantification of extracted thrombus burden characteristics and association with angiographic outcomes in patients with ST-elevation myocardial infarction: The QUEST-STEMI study. *Front. Cardiovasc. Med.* **8**, 646064 (2021).
13. Saghamanesh, S. et al. Non contrast enhanced volumetric histology of blood clots through high resolution propagation-based x-ray microtomography. *Sci. Rep.* **12**, 2778 (2022).
14. Pétré, M. *et al.* Effect of x-ray contrast-enhancing staining agents on the mechanical properties of blood vessels. In *Tomography for Scientific Advancement Society Conference (ToScA)* (2022).
15. Helfenstein-Didier, C. et al. Tensile rupture of medial arterial tissue studied by x-ray micro-tomography on stained samples. *J. Mech. Behav. Biomed. Mater.* **78**, 362–368 (2018).
16. Léonet, J. *et al.* Contrast-enhanced micro-CT protocol for in-situ mechanical experiments of aortic thrombi. In *48ème Congrès de la société de biomécanique* S125–S127 (2023).
17. Schlüter, S., Sheppard, A., Brown, K. & Wildenschild, D. Image processing of multiphase images obtained via x-ray microtomography: A review. *Water Resour. Res.* **50**, 3615–3639 (2014).
18. Berg, S., Saxena, N., Shaik, M. & Pradhan, C. Generation of ground truth images to validate micro-CT image-processing pipelines. *Lead. Edge* **37**, 412–420 (2018).
19. Phan, J., Ruspini, L. C. & Lindseth, F. Automatic segmentation tool for 3d digital rocks by deep learning. *Sci. Rep.* **11**, 19123 (2021).
20. Gasser, T. C., Görgülü, G., Folkesson, M. & Swedenborg, J. Failure properties of intraluminal thrombus in abdominal aortic aneurysm under static and pulsating mechanical loads. *J. Vasc. Surg.* **48**, 179–188 (2008).
21. Ashton, J. H., Geest, J., Simon, B. R. & Haskett, D. G. Compressive mechanical properties of the intraluminal thrombus in abdominal aortic aneurysms and fibrin-based thrombus mimics. *J. Biomech.* **42**, 197–201 (2009).
22. Schindelin, J. et al. Fiji: An open-source platform for biological-image analysis. *Nat. Methods* **9**, 676–682 (2012).
23. Brun, E., Vicente, J., Topin, F. & Occelli, R. Imorph: A 3d morphological tool to fully analyse all kind of cellular materials. *Cell. Met. Struct. Funct. Appl.* **168** (2008).
24. Gostick, J. T. et al. PoreSpy: A python toolkit for quantitative analysis of porous media images. *J. Open Source Softw.* **4**, 1296 (2019).
25. Van Aarle, W. et al. The ASTRA toolbox: A platform for advanced algorithm development in electron tomography. *Ultramicroscopy* **157**, 35–47 (2015).
26. Ostu, N. A threshold selection method from gray-level histograms. *IEEE Trans. SMC* **9**, 62 (1979).
27. Phansalkar, N., More, S., Sabale, A. & Joshi, M. Adaptive local thresholding for detection of nuclei in diversity stained cytology images. In *2011 International conference on communications and signal processing* 218–220 (IEEE, 2011).
28. Arganda-Carreras, I. et al. Trainable Weka segmentation: A machine learning tool for microscopy pixel classification. *Bioinformatics* **33**, 2424–2426 (2017).
29. Buades, A., Coll, B. & Morel, J.-M. Non-local means denoising. *Image Process. On Line* **1**, 208–212 (2011).
30. Tawfik, M. S. et al. Comparative and deep-learning denoising approaches for image-based petrophysical characterization of porous media. *Front. Water* **3**, 800369 (2022).
31. Petlitckaia, S., Vincente, J. & Poulesquen, A. Characterization of a geopolymer foam by x-ray tomography. *Front. Chem.* **9**, 754355 (2021).

32. Wang, D. H., Makaroun, M., Webster, M. W. & Vorp, D. A. Mechanical properties and microstructure of intraluminal thrombus from abdominal aortic aneurysm. *J. Biomech. Eng.* **123**, 536–539 (2001).
33. Barrett, H. E. et al. On the influence of wall calcification and intraluminal thrombus on prediction of abdominal aortic aneurysm rupture. *J. Vasc. Surg.* **67**, 1234–1246 (2018).
34. Matusik, P. et al. Architecture of intraluminal thrombus removed from abdominal aortic aneurysm. *J. Thromb. Thrombolysis* **30**, 7–9 (2010).

Acknowledgements

Author contributions

VD obtained the funding; JL, JV and VD conceived the outline of this manuscript; JL retrieved the literature; JL wrote the original draft; JL and VD edited and revised the manuscript; JL, MDM, JV, and VD approved the final version of this manuscript.

Declarations

Ethical approval

In accordance with regulations governing the storage of human tissues for scientific purposes (article L. 1243-3 of the French Public Health Code), the conservation declaration number for our study is DC-2018-3105. The study also received the ethical approval (Ref No. XJFXL8) from the research ethics committee.

Competing interests

The authors declare that the research was conducted in the absence of any commercial or financial relationships that could be construed as a potential conflict of interest.

Additional information

Correspondence and requests for materials should be addressed to V.D.

Reprints and permissions information is available at www.nature.com/reprints.

Publisher's note Springer Nature remains neutral with regard to jurisdictional claims in published maps and institutional affiliations.